Structural and Electronic Properties of Indium-Doped *n*-type Cd-Se-Te Crystals

Jing Shang[1,2] · Magesh Murugesan[1] · Rubi Gul[1,5] · Samuel Bigbee-Hansen[1,2] · Joseph M. Tallan[1,2] · Joel N. Duenow[4] · John S. McCloy[1,2,3]

Abstract

We present a comprehensive investigation into the potential of *n*-type indium-doped cadmium selenide telluride (CST:In) as a high-performance candidate for solar cell applications, without the need for resource-intensive post-growth treatments that are required for CdTe:In. We compared undoped CST and CST:In crystals under different growth conditions, analyzing their structural and electronic properties using x-ray diffraction (XRD), electron probe microanalysis (EPMA), current–voltage (IV) and Hall effect measurements, time-resolved photoluminescence (TRPL), optical transmission, and photoluminescence (PL) mapping. The results reveal that as-grown CST:In crystals achieve nearly 100% carrier activation, yielding an electron concentration of 9.5×10^{18} cm^{-3}, mobility of 653 cm^2/V·s and a 5 ns lifetime which approaches the radiative limit. Furthermore, comparison of PL maps from crystal growths having different cooling profiles suggests a strong effect of cooling rate on selenium segregation and cubic/hexagonal/polytype phase distribution. Slower cooling leads to a more homogeneous cubic structure with lower Se segregation, while a faster cooling rate results in increased Se segregation, and twin boundaries and stacking faults with polytypic and hexagonal character.

Keywords Cd-Se-Te · solar cells · time-resolved photoluminescence · Hall effect · photoluminescence mapping · crystal growth

Introduction

Cadmium telluride (CdTe) has been extensively developed and successfully applied in solar cell technology, primarily as a *p*-type absorber, where the dopant has historically been Cu or more recently As.[1,2] CdTe has an ideal bandgap (1.5 eV) which is nearly matched to the terrestrial solar spectrum and a high absorption coefficient ($\sim 10^5$ cm^{-1} near the band edge) that makes it ideal for optimal conversion efficiency[3] in single-junction solar cells. Theoretically, for a 1.5 eV gap, CdTe single-junction cell efficiency can approach 30%.[4,5] However, only recently has CdTe solar cell efficiency reached ~22.3% (arsenic-doped Cd-Se-Te),[6] with module efficiency surpassing 18%.[7] Still, the efficiency remains ~70% of the thermodynamic limit, and there is significant room to further improve the efficiency. Although the short-circuit current (J_{SC}) has reached the practically achievable limit,[8] there is still an opportunity for improving open-circuit voltage (V_{OC}) and fill factor. The major contribution to this deficit comes from the lower V_{OC} observed in CdTe cells, which has been stagnant near 850 mV, with a few notable exceptions.[9] The lower level of *p*-type doping ($p \sim 10^{14}$ cm^{-3} especially in Cu-doped materials due to compensation caused by native defects and impurities) of the absorber, and the low minority carrier lifetimes (a few ns) are considered major factors responsible for the observed lower V_{OC}. In addition, obtaining an ohmic back contact with *p*-type CdTe[10,11] is a challenge as well. There is ongoing development of

✉ John S. McCloy
john.mccloy@wsu.edu

1. Institute of Materials Research, Washington State University, Pullman, WA 99164, USA

2. School of Mechanical and Materials Engineering, Washington State University, Pullman, WA 99164, USA

3. Department of Physics and Astronomy, Washington State University, Pullman, WA 99164, USA

4. National Renewable Energy Laboratory, Golden, CO 80401, USA

5. iRay Technology, Solon, OH, USA

alternative materials to CdTe, mainly the ternary II-VI compounds, Cd-Ze-Te (CZT) and Cd-Se-Te (CST), with group V (P, As, Sb), group III (Al, Ga, In), and group VII (Cl, I) elements incorporated as dopants. In this paper the focus is on CST with indium doping, leading to *n*-type material.

With the addition of Se, a substantial reduction in the bandgap of CdTe has been demonstrated, decreasing from 1.5 eV to 1.39 eV (CdSe$_{0.4}$Te$_{0.6}$).[12] This increases absorption in the long wavelength part of the spectrum and improves the device J$_{SC}$ and fill factor,[13–15] resulting in a net increase in efficiency of the solar cell. In the recent past, efficiency has been increased from 19.5% to 22.1% by the addition of selenium to the front of the CdTe absorber layer.[16] CST has been reported to be highly uniform and homogeneous,[17] as the segregation coefficient (*k*) of Se in CdTe is $k_{Se} \leq 1$.[18] However, the crystals investigated by this group had Se $\leq 10\%$ on the anion site as opposed to 40% here. The binding energy of Cd-Se is 1.3 times higher than Cd-Te and the lattice constant of CdSe is 0.9 times that of CdTe.[19] This provides less chance to generate Cd vacancies in CST crystals as compared to CdTe.[20]

While most of the published research has focused on *p*-type doping of CdTe/CST, there has been some work on *n*-type doped CdTe via dopants such as indium.[21,22] Under Te-rich stoichiometry conditions, indium can be easily incorporated. However, it is well known that highly *n*-type bulk crystals are difficult to obtain due to self-compensating defect formation. Bulk crystals doped with donors result in high resistivity due to the formation of donor–acceptor (In$_{Cd}$–V$_{Cd}$) defect complexes known as A-centers.[23] However, for CdTe:In, it was found that annealing in Cd produced high activation, and thus high electron carrier concentration.[24] Considering the intricate connections to the CdTe-In phase diagram, segregation behavior in CdTe, and the diffusion solubility in CdTe,[25] the goal is to achieve the maximum uncompensated doping with donors within the range of 10^{18}–10^{20} cm^{-3}.[21,25,26,26–31] In our investigation, aiming for the highest feasible dopant level, we have selected 10^{19} cm^{-3} and 10^{20} cm^{-3} as the doping levels for our experimental work.

In this paper, we discuss the bulk growth and characterization of the CST ternary compound with a 60%/40% nominal Te/Se concentration. We show that *n*-type doped CST crystals, for absorber or emitter applications in homo- or heterojunctions, were achieved by adding indium to the starting material. Bulk crystals were grown using modified vertical Bridgman and high-pressure Bridgman techniques. The ultimate goal is to use these pre-doped crystals as feedstock for the production of thin film photovoltaic absorbers.[32]

The grown crystals of CST, both In-doped and undoped, were characterized by several techniques. The electronic properties and optical properties were investigated by Hall effect measurements, time-resolved photoluminescence (TRPL), and near-infrared transmission. In the targeted application, crystals will be ground to powdered feedstock; nonetheless, we wanted to assess the compositional homogeneity of the grown crystals. This was done via a combination of electron probe microanalysis (EPMA), photoluminescence (PL) mapping, and X-ray diffraction (XRD).

Experimental Procedures

Crystal Growth

Bulk ingots of undoped and indium-doped CdSe$_{0.4}$Te$_{0.6}$ (CST) were grown by using the vertical gradient freezing (VGF) method in a modified vertical Bridgman (MVB) furnace, where thermal gradients were controlled electronically, and the ingots did not move. For comparison, a high-pressure Bridgman (HPB) crystal growth was performed for an undoped CST crystal. The list of the CST crystal growths and some details are provided in Table I.

Crystals were batched using 6N (99.9999%) high purity CdTe and 5N (99.999%) purity of CdSe combined with elemental indium (In) for doped crystals, with dopant levels from ~1×10^{19} to 1.5×10^{20} cm^{-3}. The charge preparation was performed inside a bag with flowing argon in a class 1000 clean room facility, in order to minimize contamination. Silica ampoules, as well as a pyrolytic boron nitride (pBN) crucible and lid if used, were etched with 20%

Table I Details on CST crystal growths

No.	Identifier	Dopant	Batched (cm^{-3})	GDMS (cm^{-3})	Growth conditions	Crucible	Growth rate (mm/h)	Ingot mass (g)
CG-237	UID-Mp	None	–	–	MVB-ACRT	pBN	1	766
HPB-5	UID-Hp	None	–	–	HPB	pBN	900	575
CG-244	InH-M0	In	1.8×10^{20}	9.7×10^{18}	MVB	None	1	459
CG-248	InL-M0	In	1.5×10^{19}	n.m.	MVB	None	1	459
CG-229	InL-Mp	In	1.5×10^{19}	8.0×10^{17}	MVB	pBN	1	459

n.m., indicates not measured.

hydrofluoric acid solution for 20 min. The batches were placed in the clean ampoules, which were then sealed under high vacuum of ~10^{-9} kPa using a rotary torch, and the seals checked using cross polarizers. When the ampoule containing the batch was ready, it was carefully aligned and loaded into the furnace.

For VGF growth, the maximum temperature was maintained at 1150°C. The temperature gradient was kept at 50°C and the growth rate was 1 mm/h. For a typical ingot weight (~450–800 g), the growth takes about 13 days. The diameter and length of the ingots grown are typically 60 mm and 70–100 mm, respectively. Some of the VGF growths used the accelerated crucible rotation technique (ACRT), which is a melt-stirring technique involving periodic, but not constant, rotation of the crucible holding the melt. ACRT-induced flows can significantly reduce thermal and compositional inhomogeneity that occur in static growth conditions.[20] ACRT rotation rates up to 30 rpm were applied to selected VGF crystals.

For the HPB growth of undoped CST, a conical high-purity graphite holder of 4-inch inner diameter and 15-inch height was used for crystal growth after a vacuum bake-out. Source materials were placed in a pyrolytic boron nitride (pBN) crucible, which was inserted into the silica ampoule, then placed into the graphite holder. The ampoule containing the batch was heated to 1160°C at a heating rate of ~80–100°C/h. The chamber pressure gradually increased from 60 atm at room temperature to ~80 atm at the maximum furnace temperature of 1160°C. A ~575 g undoped crystal was grown using CdSe and CdTe raw materials, at a growth rate ~900 mm/h, and the total process time was 28 h. More details on the HPB processes can be found elsewhere.[32]

For ease of interpretation, growths in Table I are denoted by an abbreviation. The abbreviation comprises the doping levels (first three letters), growth method (the fourth letter), and the crucible type (the fifth letter). Doping levels are indicated as follows: "UID" for undoped, "InL" for low indium doping level (~10^{19} cm^{-3}), and "InH" for high indium doping level (~10^{20} cm^{-3}). The growth methods are represented by "H" for high-pressure Bridgman and "M" for modified vertical Bridgman, while the crucible types are denoted by "p" for pBN and "0" for none. As an example, CG229 is doped with an In concentration of 10^{19} cm^{-3} and fabricated using the MVB method with a "pBN" crucible, referred to as "InL-Mp".

Sample Preparation

After removal from the furnace, crystals were removed from the ampoule and weighed; then ingots were sand blasted, cleaned, and reweighed. The crystal appearance was studied closely. Ingots were then cut into ~2-mm-thick axial (from the middle bulk region) and radial wafers (from the heel and tip) using a wire saw. After marking the visible grain boundaries, each wafer was further cut into approximately $10 \times 10 \times 1$ mm^3 samples to minimize the presence of grain boundaries in each sample. Then the samples were polished with Al_2O_3 suspension and further cleaned with deionized water and ethanol/ methanol. For bulk electrical characterization, selected crystals were polished on all six sides; alternatively, for use as substrates or for structure and morphology characterizations, only two sides were polished.

Prior to PL mapping and EPMA, samples were etched in Br-methanol solution for 2 min. On bulk wafers, contacts were fabricated using different procedures, including sputtering and different time-temperature recipes on a hotplate. For Hall experiments, the 4-point contacts were made ~1 mm in diameter at the corners, either Au or In dot contacts. For IV measurements, 2-point planar Au contacts were fabricated using sputtering.

Characterization

Doping and impurity levels in the CST crystals were checked on selected samples using glow discharge mass spectrometry (GDMS), performed at the National Research Council, Canada. The crystal structure was confirmed using a powder X-ray diffractometer (PANalytical X'Pert Pro) with a Cu K alpha source and semiconductor detector. Scans were performed from 10° to 90° 2θ with step size of 0.01° and 10 s per step. Local chemistry was checked with an electron microprobe (JEOL JXA-8500F) using electron probe micro-analysis (EPMA) with wavelength dispersive spectroscopy (WDS) for elemental quantification.

For optoelectronic property measurements, near-infrared (NIR) transmittance, current–voltage (I–V) curves, Hall effect, and two-photon excitation time-resolved photoluminescence (2PE-TRPL) were performed. NIR transmittance, how much near-infrared light passes through the crystal, was measured on an Agilent Cary 5 spectrometer. The absorption spectra and optical bandgap were calculated using methods described previously.[33,34]

I–V measurements were performed with a Keithley 6487 picoammeter using the two-probe method and Au sputtered planar contacts. Hall measurements were performed in standard four-wire configuration on polished samples with Au contacts using an MMR Hall measurement system with a 1.4 T magnet, or at the National Renewable Energy Laboratory (NREL) using an Accent HL5500PC with a 0.31 T magnet and In soldered contacts.

TRPL measurements were performed to measure the bulk minority carrier lifetime. Since CdTe-based compounds have high surface recombination velocity, 2 photon excitation (2PE) was used to sample the bulk crystals, with the focus being ~10 μm below the surface and ~300 μm wide.

A mode-locked, 200-fs-pulse-width laser firing $\approx 1.1 \times 10^6$ pulses per second with a tunable-wavelength optical parametric amplifier was used to generate 1120 nm laser light. Approximately 8–10 mW was focused on the sample using a microscope objective which varied from 20× to 60×. A PicoQuant PicoHarp 300 time-correlated single-photon counting system collected the TRPL data. A dichroic with $R = 1020$–1550 nm and $T = 520$–985 nm was used, with a bandpass filter centered at 819 nm.

Photoluminescence (PL) mapping was conducted over the same large area to identify any emission changes associated with the microstructure. A spatially resolved PL map was generated using a Klar Mega Pro microscope equipped with a 635 nm continuous wave laser and Ocean Insight Maya2000 Pro spectrometer. Spectra were collected at room temperature using a spatial step size of 50 μm. Spectral fitting was performed using graphics processing unit (GPU) accelerated fitting. A custom model consisting of Gaussian and bi-Gaussian functions was used to match the observed spectral features of the sample. Maps of the fitted spectral parameters were then plotted as a false-color image.

Results and Discussion

Crystal Appearance

A preliminary visual inspection of the crystal morphology, size, and homogeneity was conducted on the sand-blasted as-grown ingots, whose corresponding photographic images are shown in Fig. 1. Notably, CG-237 (UID-Mp, Fig. 1a) has no added intentional dopant and exhibited large grain size
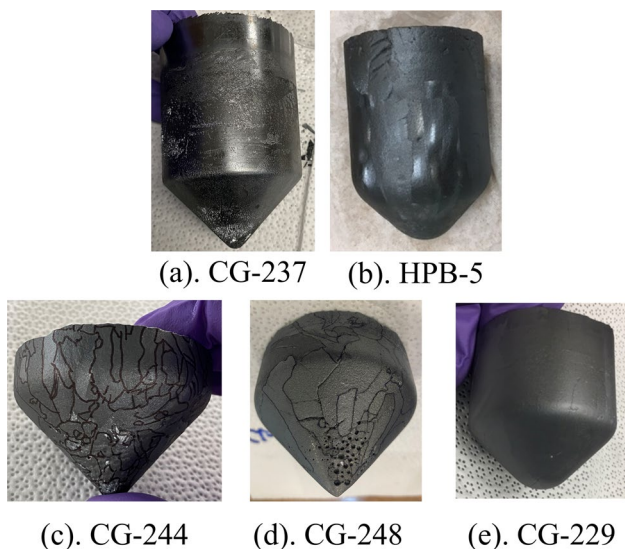

Fig. 1 Photos of ingots for (a) CG-237/ UID-Mp, (b) HPB-5 /UID-Hp, (c) CG-244/ InH-M0, (d) CG-248/ InL-M0, (e) CG-229/InL-Mp.

with comparatively uniform and homogeneous growth quality. In contrast, due to the high growth rate, HPB-5 (UID-Hp, Fig. 1b) exhibited a highly polycrystalline nature. Furthermore, CG-244 (InH-M0, Fig. 1c), which incorporated a relatively elevated concentration of In dopant, exhibited a distinctively polycrystalline nature. Conversely, CG-248 (InL-M0, Fig. 1d), featuring a reduction in the In dopant concentration, demonstrated an enlargement in grain size with a heterogeneous mixture of large and medium-sized grains. Additionally, certain regions at the tip exhibited porosity. The utilization of a pBN crucible led to notable improvements, including porosity reduction and larger grains. CG-229 (InL-Mp, Fig. 1e) exhibited a configuration characterized by substantial grain enlargement, resulting in a comparatively superior and uniform crystal growth quality.

Comparing the crystal quality of these growths, we observe that high growth rates and increased dopant concentrations lead to a more polycrystalline structure. On the other hand, aiming for low growth rates and minimal dopant levels does not necessarily ensure single crystallinity. However, using a pBN crucible within the fused quartz ampoule visibly improves crystal quality. This improvement is linked to better uniformity and homogeneity, ultimately resulting in a higher yield of single crystals.

Structural Properties

Figure 2 displays the XRD patterns of CST and CdTe:In (CG-191)[24] for reference. In the XRD patterns of CST, a noticeable shift towards higher 2θ angles is observed when compared to pure CdTe. Pure CdTe exhibits a diffraction peak at approximately 23.7–23.8°, which corresponds to the (111) close packing planes of the cubic structure. Pure CdSe shows a hexagonal crystal structure with a preferential
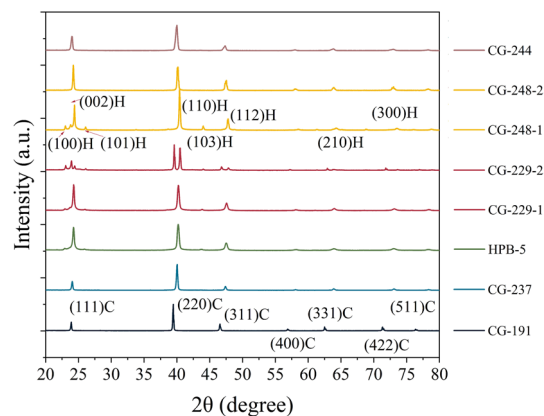

Fig. 2 XRD patterns of undoped (CG-237/UID-Mp and HPB-5/UID-Hp) and indium-doped CST (CG-244/InH-M0, CG-248/InL-M0, CG-229/InL-Mp) with reference of CdTe:In (CG-191) [24]. Planes are labeled indicating the H (hexagonal) or C (cubic) phase.

oriented peak for (0001) at 25.25°.[35] With the introduction of CdSe into CdTe, the peak shifts to the range of 23.9°–24.4° and occasionally displays splitting (as observed in CG-229-2) or shoulders (as seen in HPB-5), suggesting the presence of polytype. This behavior was also reported in CST thin films,[35] and in previous crystals (see below). Furthermore, In doping does not induce obviously structural changes because the impurity level is too low.

At room temperature, CdTe is a cubic zincblende crystal structure while CdSe is a hexagonal wurtzite structure.[36] In previous studies of bulk crystal growth in the CdSe-CdTe binary,[36] it was observed that crystals with < 40 mol.% CdSe have the cubic structure, those with > 70 mol.% CdSe have the hexagonal structure, and those in between can have either structure. It was also reported that furnace cooled ingots with 40–50 mol.% CdSe could produce an unidentified polytype consisting of mixed cubic and hexagonal stacking. This tendency leads to the production of polytypes, which are crystals with repeated stacking on the < 111 > cubic or < 0001 > hexagonal close-packed directions with repeat sequences of 6 to > 70 (as opposed to two in hexagonal wurtzite or three in cubic zincblende), and are common in some binary II-VI semiconductors (ZnS) as well as some III-V semiconductors (SiC).[37–39] In ternary semiconductors this has also been observed, as for Cd-Se-Te,[36] but not Cd-S-Te.[40] In practice, it is difficult using only powder X-ray diffraction to distinguish true polytypes (i.e., repeating long-period stacking sequences of mixed cubic and hexagonal layers) from "stacking faults" (i.e., occasional hexagonal stacking in primary cubic matrix) and twins (i.e., single hexagonal layers between cubic regions) in zincblende/wurtzite systems. Unambiguous determination requires single crystal X-ray diffraction or transmission electron microscopy, which was not conducted here.

Optical and Electronic Properties

Transmission measurements were performed on ~1-mm-thick samples to measure the optical band edge (E_{opt}) of undoped (CG-237/UID-Mp and HPB-5/UID-Hp) and indium-doped (CG-229/InL-Mp and CG-244/ InH-M0) CST. Figure 3 shows the optical transmission spectra, calculated absorption spectra, and optical band edge as obtained by first derivatives, as described in Refs. 33, 34. The band edge E_{opt} of undoped CST is 1.33 eV, while the low-doped CST is 1.38 eV and high-doped CST is 1.45 eV. For undoped CST, it is generally agreed in the literature that the smallest E_{opt} in the CdTe-CdSe binary is at the $CdSe_{0.4}Te_{0.6}$ composition, the same composition used here, but our value differs from those previously reported. Thin film energy gap values for this composition have been reported at 1.50 eV[41] or 1.39 eV.[12,42] The value obtained here is properly the effective optical gap and contains the Urbach tail since the samples
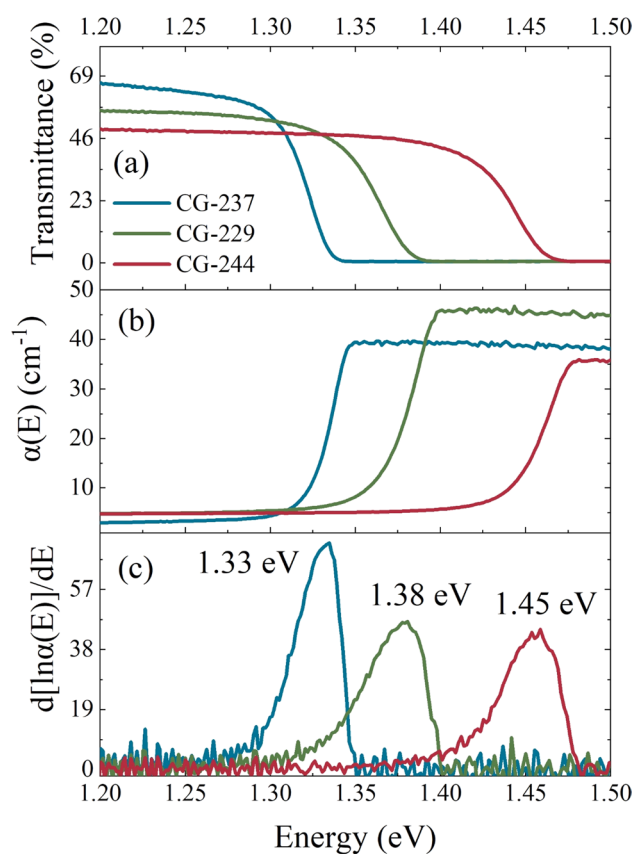

Fig. 3 Optical gap determined by (a) transmission spectra measured for ~1 mm CST samples: undoped (CG-237/UID-Mp) and indium-doped (CG-229/ InL-Mp and CG244/ InH-M0) CST; (b) absorption coefficient α(E); (c) the energy derivative of the logarithmic absorption coefficient, d[lnα(E)]/dE.

were ~1 mm thick. Furthermore, the introduction of indium doping results in an elevated concentration of impurities and defects, leading to an increased free carrier density within the bands. This phenomenon induces the formation of band tails and variations in the density of states. Consequently, one would expect a decreasing trend in the optical band-gap values with increasing indium doping. However, in our case, indium doping causes an increase in bandgap values. This could be explained by indium doping leading to the formation of smaller grain size, more grain boundaries, and a decrease in selenium concentration, which aligns with the results of the PL bandgap, as we will discuss later. Similar trends were observed in indium-doped CdSe thin films.[43]

I–V characteristic plots are shown in Fig. 4a, with data in Table II. In the plot, the indium-doped samples CST:In exhibit a high dark current. In contrast, the undoped crystals (CG-237/UID-Mp) exhibited a resistivity of ~6 × 10^6 Ω·cm, while CST:In (CG-229/InL-Mp) displays resistivity < 1 Ω·cm. The resistivity of CST:In decreased by six orders of magnitude compared to undoped CST, suggesting indium doping induced a significant increase in conductivity.

Fig. 4 *I–V* characteristic plots (a) for as-grown crystals including CG-237/UID-Mp, CG-244/InH-M0, CG-248/InL-M0, and CG-229/InL-Mp; and (b) for CG-229/InL-Mp annealed with an overpressure of Se.
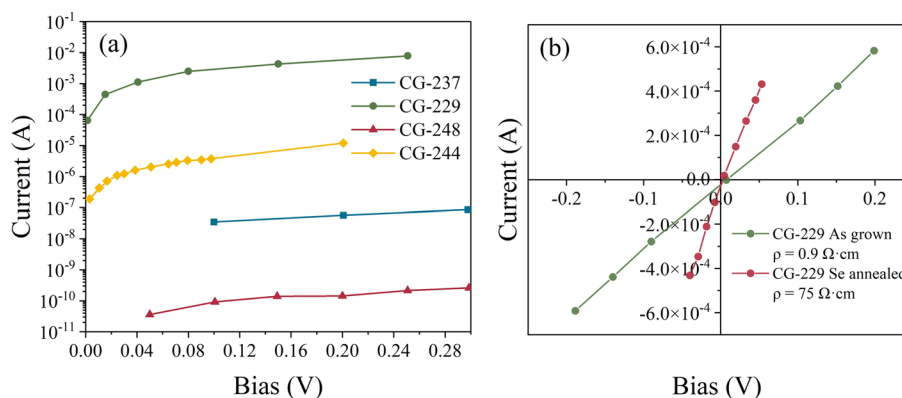

Table II Electrical properties of selected CST crystals

	CG-237			CG-229			CG-244		
Batched In (cm^{-3})	Undoped			$\approx 10^{19}$			$\approx 10^{20}$		
GDMS In (cm^{-3})	NA			$\approx 10^{18}$			$\approx 10^{19}$		
Crystal type	Poly-	Single	Single	Poly-	Single	Single	Poly-	Single	Single
Contacts	Au	Au	In	Au	Au	In	Au	Au	In
ρ(Ω·cm)–IV	NA	6×10^6	NA	NA	$<10^0$	NA	NA	$<10^{-1}$	NA
ρ(Ω·cm)–Hall	3.82×10^7	2.02×10^7	1.13×10^9	6.27	6	6.3×10^{-3}	0.28	0.08	2.2×10^{-3}
μ(cm^2/V·s)	0.622	6.19	13.5	104	2×10^3	419	85	232	365–653
Density (cm^{-3})	9.9×10^{10}	5.8×10^{10}	4.1×10^{10}	1.3×10^{16}	5.0×10^{15}	4×10^{18}	1.6×10^{17}	1.9×10^{18}	$(5.5\text{–}9.5)\times10^{18}$

For resistivity measurements, different types of contacts were performed: In contacts were soldered and Au contacts were sputtered. Polycrystalline (Poly-) values are provided for samples with mixed grain structures.

To further confirm that the observed *n*-type conductivity in CST:In is due to indium rather than selenium vacancies, we conducted annealing in a selenium atmosphere at ~5×10^{-2} atm for CST:In (CG-229 /InL-Mp). Hypothetically, if the high conductivity is caused by selenium vacancies, the resistivity of CST:In would drop significantly due to filling of the selenium vacancies. However, selenium annealing of CST:In resulted in a two-orders-of-magnitude increase in resistivity, from 0.9 Ω·cm before to 75 Ω·cm after (see Fig. 4b). This suggests that In doping is the main cause of the conductivity increase, and any contribution of selenium vacancies to the conductivity is minor.

Hall effect experiments were conducted using Au and In contacts, and the data for resistivity, mobility, and carrier concentrations are presented in Table II. In doping significantly decreases resistivity while increasing both mobility and carrier density as compared to undoped CST. Comparing single crystals (samples with a single grain) and poly crystals (samples with multiple grains), we found that single crystals show lower resistivity and higher mobility, which results from the absence of grain boundaries. The exception is CG-229, presumably due to more carrier scattering. Finally, comparing Au and In contacts, the doped samples

with In contacts are more conductive and showed lower resistivity and higher carrier density; the unintuitive higher resistivity from the undoped sample with indium (vs. gold) contacts probably results from the large errors in measurements of high resistivity due to small amounts of current.[44] Also, given the calculated values of electron affinity and bandgap of CdSe$_{0.4}$Te$_{0.6}$ of 4.7 eV and 1.4 eV,[45] Au contacts (work function 5.3–5.47 eV[46,47]) should be Schottky contacts for CST while In contacts (work function 4.09 eV[46]) should be ohmic for CST. Thus, for these measurements, the measurements with indium contacts should be the more reliable ones.

Additional Hall measurements were performed with In contacts on the same crystals, as In contacts were more likely to be ohmic. Data were collected under several conditions for CG-244/InH-M0. As-grown samples were measured with pressed In contacts as well as soldered In contacts. For pressed In contacts, the average values for five measurements were $\rho=2.21\times10^{-3}$ Ω·cm, $\mu=365$ cm^2/V·s, and $n=9.6\times10^{18}$ cm^{-3}. For soldered indium contacts, the average of three measurements were $\rho=2.23\times10^{-3}$ Ω·cm, $\mu=653$ cm^2/V·s, and $n=5.5\times10^{18}$ cm^{-3}. A slightly lower contact resistance was observed with the soldered In wires (2

Ω across sample for soldered In versus 3–4 Ω for pressed In). Note that the difference here in extracted properties is about a factor of 2 in mobility (larger for soldered contacts) and half in carrier concentration (lower for soldered contacts).

In conclusion, when accounting for the impact of contacts on resistivity and mobility, the properties for CG-244/ InH-M0 can be summarized as $\rho \approx 10^{-3}$ Ω·cm, $\mu = 232$–865 cm^2/V·s, and $n = (2$–$10) \times 10^{18}$ cm^{-3}, meaning that the activation for In detected by GDMS is 20–100% in this sample. Generally, the In soldered contact Hall measurements showed the lowest resistivities and highest carrier concentrations with the most reasonable mobilities and are probably closest to the real values. However, the undoped CST has high resistivity and the Hall results were somewhat suspect, though the resistivity values agreed well with I–V methods.

2PE-TRPL measurements were conducted on selected samples to determine carrier lifetimes, as depicted in Fig. 5. The undoped CST (HPB-5/UID-Hp) exhibited a lifetime of 13.3 ns. In contrast, the low indium-doped CST (CG-229/InL-Mp) had a shorter lifetime of 1.5 ns. For the high indium-doped CST (CG-244/InH-M0), as-grown, the lifetime measured between 0.34-0.42 ns.

We plotted the radiative combination rate (τ_R), which for low-injection conditions, such as performed in these 2PE-TRPL experiments, is $\tau_R = 1/(Bn)$, where B is the radiative recombination rate coefficient (here chosen as 1×10^{-10} cm^3/ s[24] as used for CdTe), and n is the carrier concentration. Calculations were performed for measured values in CST:In and undoped CST and compared to published results for CdTe:In[24] (Fig. 5e).

Other than the undoped material, which is far from the line representing lifetime limited only by recombination, the CST materials behave much better than CdTe:In, which required a Cd anneal to activate sufficient dopant atoms to increase the carrier concentration to near the radiative limit. Apparently, the A-center acceptor defect composed of a cadmium vacancy and donor complex, here V_{Cd}-In$_{Cd}$, is not as much of a problem in CST as it is in CdTe, and therefore a Cd treatment is not required for CST to achieve high activation. By contrast, the results on undoped CST suggest a high density of Shockley–Read–Hall (SRH) recombination centers (in HPB-5/UID-Hp), which may be related to electronic disorder in Cd-Se-Te.[48]

Photoluminescence Mapping

The axial compositional uniformity for the CST crystal was studied by mapping the photoluminescence (PL) spectra. The spatial distribution of PL energy peak positions, E (eV), serves as an indicator of compositional variation and, consequently, the bandgap of the material. This analysis was conducted on undoped CST (CG-237), low-doped CST:In
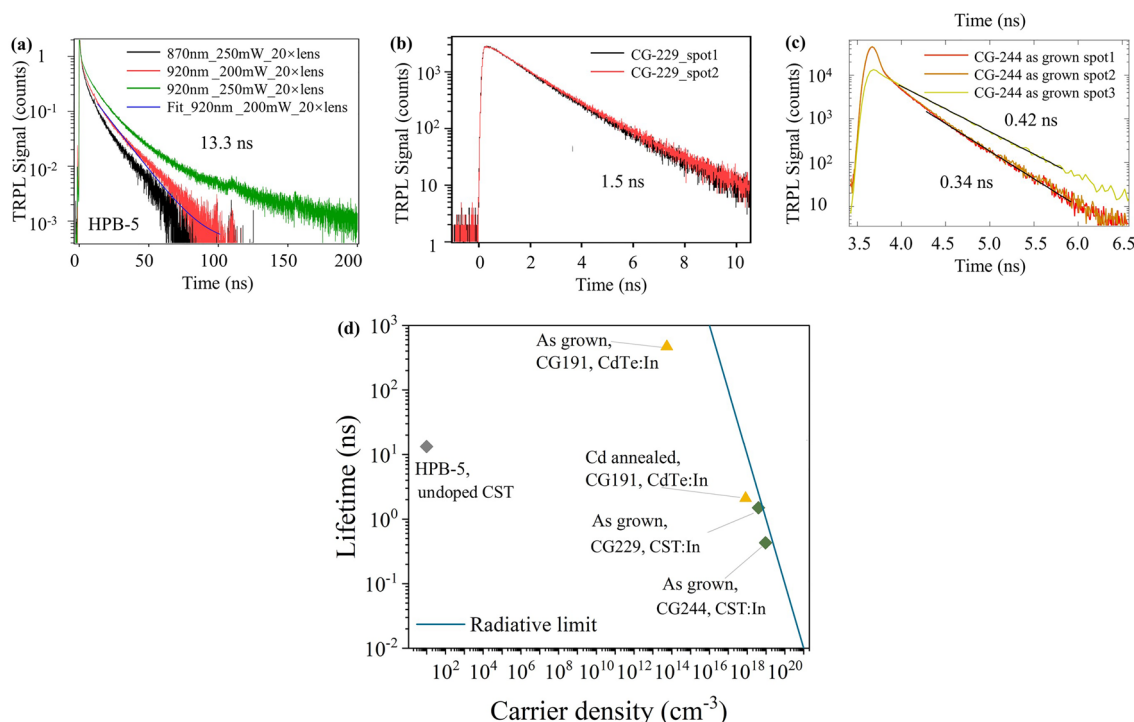

Fig. 5 2PE-TRPL measurements of (a) undoped CST (HPB-5/UID-Hp); (b) low-doped In:CST (CG-229/InL-Mp); (c) high-doped In:CST (CG-244/InH-M0); (d) radiative lifetime and carrier density ideal relationship shown as a blue line and for CST and CdTe:In (CG-191) (Color figure online).

(CG-248), and high-doped CST:In (CG-244) samples, allowing for a comparative study.

Figure 6 illustrates the PL mapping results for the undoped CST sample (CG-237/UID-Mp), showing PL emission spectra, PL peak energy mapping, and PL intensity mapping. Figure 6a shows the wafer used for PL measurements, while Fig. 6b depicts a single observed energy peak. Additionally, PL energy and intensity mapping images are presented in Fig. 6c and 6d, respectively. The full range of the change in the peak energy is between ≈1.39–1.40 eV, which confirms the compositional uniformity for the as-grown CST. Note that this value is significantly higher than the optical gap obtained by transmission measurement, as expected, and is closer to the true electronic bandgap for CST. The intensity mapping shows large grains with a few twins along the growth direction, which are emerging from the lower right side of the wafer.

In the higher indium-doped CST (CG-244/ InH-M0), as shown in Fig. 7, ≈1 million PL spectra were analyzed using a three-component fit, comprising one Gaussian and two bi-Gaussian functions. The majority peak was ≈1.41 eV, with some higher energies manifesting near the shoulders of the conical crystal, to ≈1.46 eV. Along the axial direction from the tip, the PL was very homogeneous. The intensity map highlighted some indication of the grain boundaries, particularly in the widest region away from the tip, as

well as some different grains at the shoulders. These grains were clearly observed when plotting the low energy peak (≈1.26–1.28 eV). The middle energy peak (≈1.34–1.36 eV) gave a picture similar to the main peak.

Figure 8 presents the behavior of low-doped CST:In (CG-248) through maps derived from the analysis of over a million spectra, featuring a predominant single domain peak. These maps reveal intricate patterns with sharp transitions. Across most regions, except along the outer crystal surface (the first to freeze) and the heel of the crystal (the last to freeze), the PL peak energy falls within ≈1.40–1.44 eV. Notably, the conical region displays a mixture of single and polycrystalline material, while above the shoulder, the crystal appears remarkably homogeneous. Moreover, the intensity maps suggested some grain boundaries and twins aggregating along grain boundaries.

Discussion

The Influence of Se Concentration and Structural Factors on PL Bandgap

Given the intricate behavior exhibited by CST:In, a critical question arises: Does the PL energy level result from variations in Se or In concentration or structural differences?

Fig. 6 PL measurements of (a) wafer used, (b) energy intensity spectrum, (c) intensity mapping, (d) energy mapping of undoped CST (CG-237/UID-Mp).
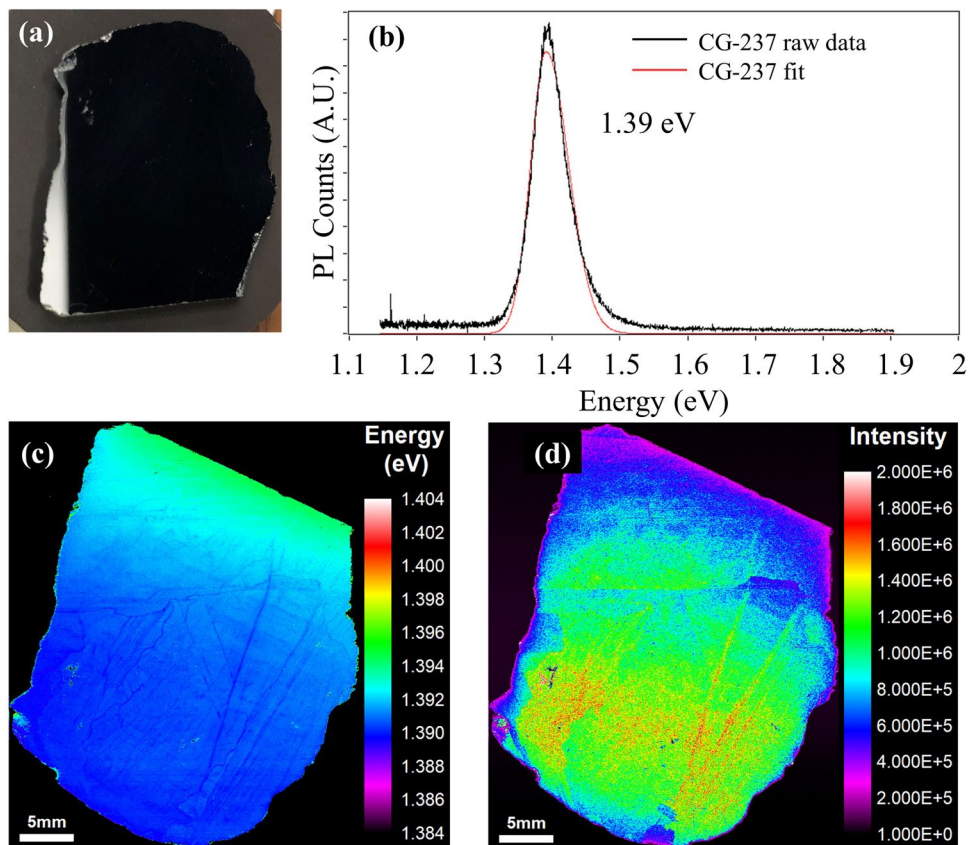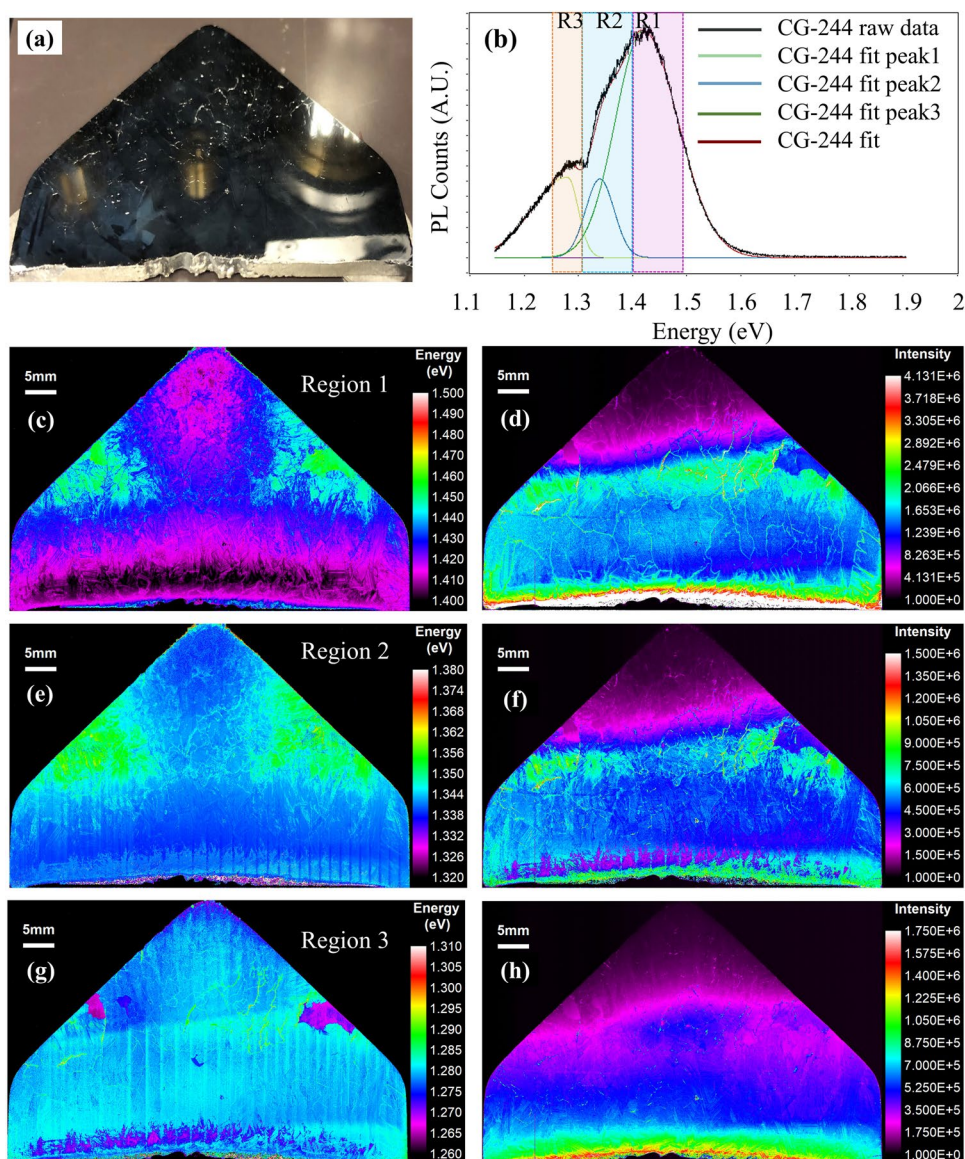
Fig. 7 PL measurements of high-doped CST (CG-244/InH-M0) (a) The sample used; (b) PL spectra summarized; (c) PL energy and (d) intensity mapping in energy region 1 from 1.4 eV to 1.5 eV; (e) PL energy and (f) intensity mapping in energy region 2 from 1.32 eV to 1.38 eV; (g) PL energy and (h) intensity mapping in energy region 3 from 1.26 eV to 1.31 eV.

To address this question, Fig. 9 presents detailed PL mapping, XRD, and EPMA data for CG-248/ InL-M0, offering insights into the underlying factors.

An attempt was made to correlate the PL energy with selenium concentration in the PL maps, using the relationship x(Se mole fraction) = A(E_{gap}(CdTe)-E_{PL}), as suggested by.[49] Here, $A = 2.596$ and E_{gap}(CdTe) $= 1.502$ eV on this PL system. The mapped results are shown in Fig. 9c. The calculated Se concentration variations seemed high ($x \approx 0.11$–0.28, where the target value was 0.40).

Furthermore, we conducted EPMA analysis on several selected regions, as indicated in Fig. 9a, with the corresponding EPMA results presented in Fig. 9d to i. These analyses revealed a Se concentration range of 0.15 to 0.25. Interestingly, these results align closely with the calculated Se concentration based on the PL bandgap, which falls within

the range of 0.11 to 0.28. For instance, when comparing the PL bandgap values of 1.4 eV and 1.44 eV, the calculated Se concentrations are 0.26 and 0.16, respectively. In the EPMA measurements, these correspond to ranges of 0.21~0.19 and 0.17~0.15 according to Fig. 9f.

Comparing sections 1 and 2 with section 3, based on the calculated Se concentration using the PL bandgap, one would expect lower Se concentrations in the former regions. However, EPMA analysis reveals higher Se concentrations in both sections 1 and 2. These findings underscore that the PL bandgap is influenced not solely by Se concentration but also by structural properties, such as the presence of planar and linear defects such as twin boundaries and stacking faults.

Moreover, to explore structural details, XRD powder measurements were carried out on subsamples from

Fig. 8 PL measurements of low-doped CST (CG-248/InL-M0) (a) The sample used; (b) PL energy mapping and (c) intensity mapping; (d) the PL spectrum in the blue region in energy mapping; (e) the PL spectrum on the grain boundary in intensity mapping.
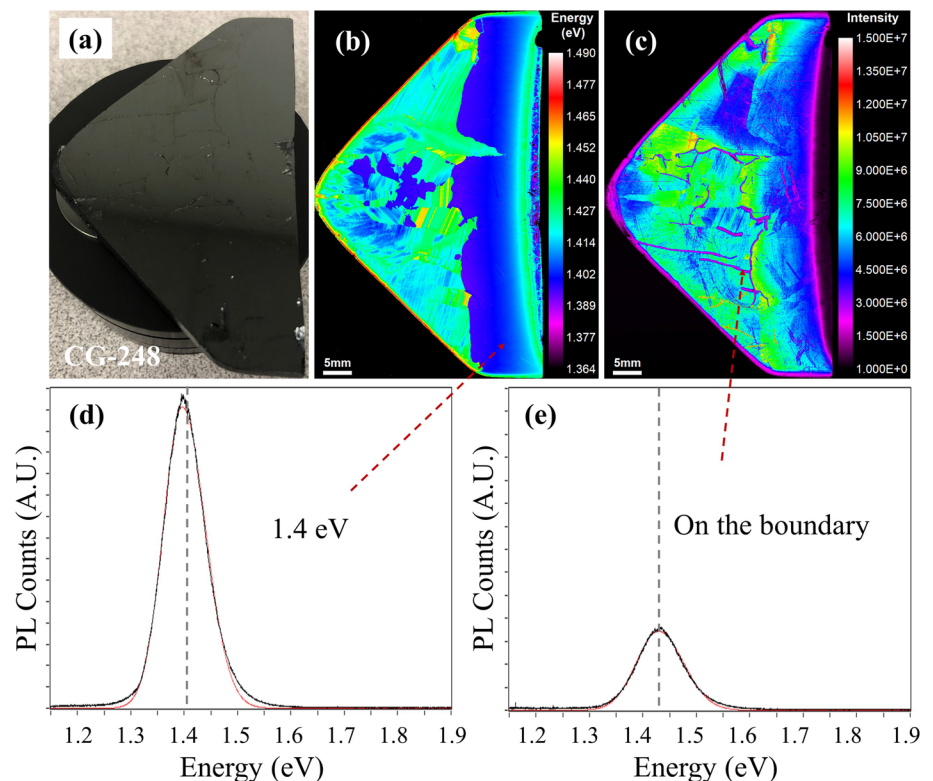
sections 1 to 8, with their locations indicated in Fig. 9b. The XRD data can be found in Fig. 9j and k. Notably, the cubic (111) peak, typically centered at 24.5°, exhibited an intriguing shift to lower 2θ values when going from the tip (24.38°) to the shoulder (24.22°) in ingot CG-248/InL-M0. Furthermore, within the tip area up to the shoulder, additional polytype peaks appeared (23.01° ~ 22.96°, 23.79° ~ 23.76°, and 26.07° ~ 26.03°). However, these peaks vanished in sections 6 to 8, where the PL bandgap remained uniform at 1.4 eV. One reasonable explanation is the shift in Se concentration, supported by EPMA results, transitioning from high to low from tip to shoulder region.

Besides Se segregation, another explanation is that these diffraction results do not indicate polytypes or hexagonal phase, but rather a level of "hexagonality."[50] This hexagonality can be attributed primarily to the presence of twin boundaries and stacking faults, which may arise due to different thermal profiles during the cooling process. These structural variations could result from the delicate balance between hexagonal, cubic, and mixed (polytype) stacking, particularly at the 40% CdSe Cd-Se-Te composition. The crystal may undergo mixed wurtzite and zinc-blende phases or polytypes, contingent upon the cooling process following growth, as depicted in the phase diagram.[36] If the crystal experiences rapid cooling to room temperature, it may retain some hexagonal phase characteristics, which are more pronounced in the tip region than at the heel.

In summary, differences in cooling temperature and Se concentration can both impact the structure of Cd-Se-Te crystals and influence the PL bandgap. A slower cooling rate leads to a more homogeneous cubic structure with lower Se segregation, while a faster cooling rate results in increased Se segregation and hexagonal structure with twin boundaries and stacking faults. However, the specific mechanisms and quantitative calculation through which each defect or phase affects the PL bandgap are still under investigation.

Conclusion

In this research, the undoped and In-doped CST grown with different methods are investigated thoroughly. First and foremost, CST crystals exhibit ideal electronic properties. The grown CST:In crystals demonstrate up to 100% carrier activation without post-growth treatments, resulting in a carrier concentration of 9.5×10^{18} cm^{-3}, mobility of 653 cm^2/V·s and a 5 ns lifetime—approaching the radiative limit for this material. What sets CST crystals apart is their ability to achieve this level of activation with *n*-type charge carriers, all without the need for additional and resource-intensive heat treatments such as Cd- and CdCl$_2$-annealing. This not only simplifies the production process but also translates to significant savings in terms of time, expenses, and labor.

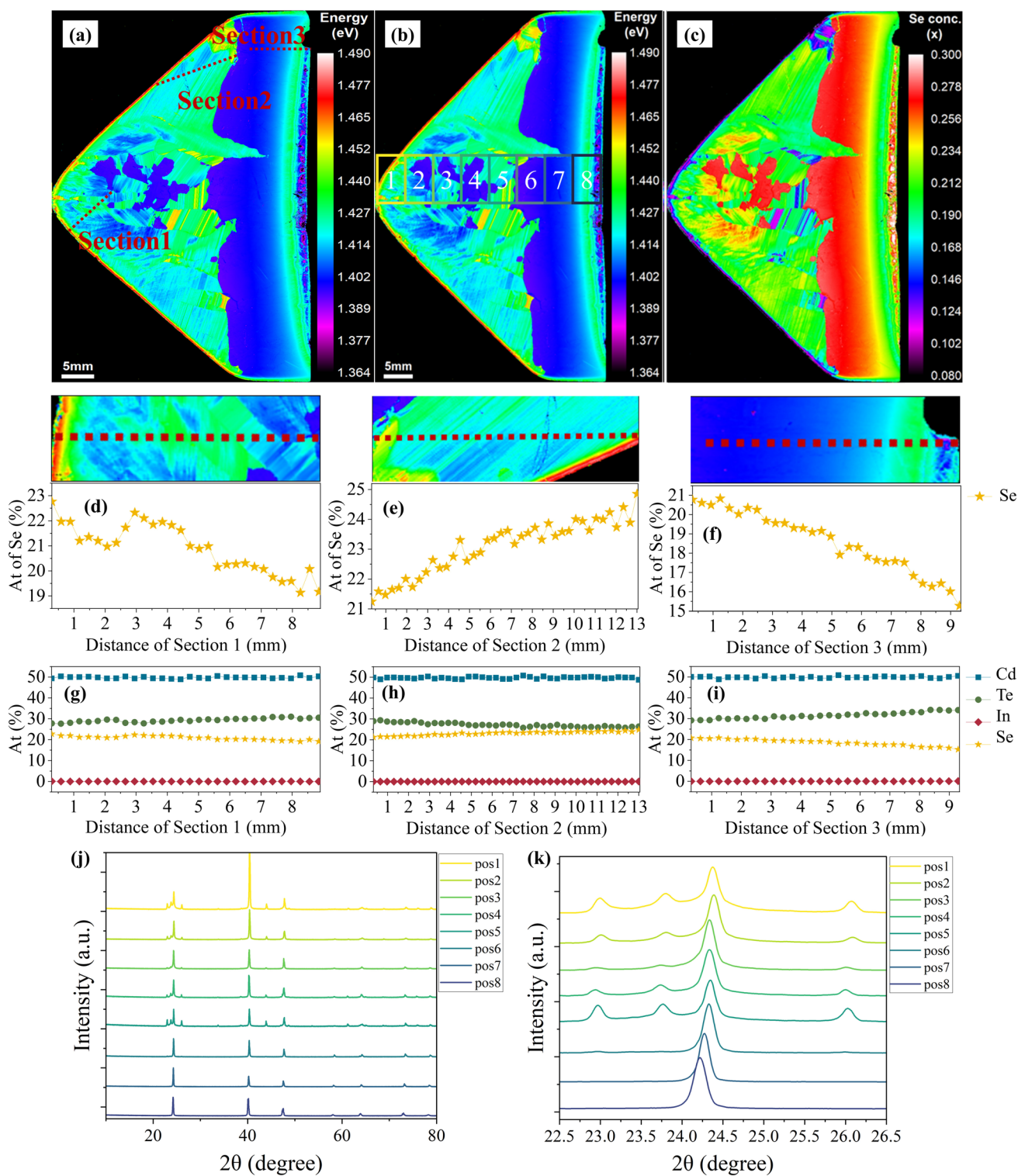Furthermore, this study explores detailed PL mapping and its underlying causes, including Se concentration and

Fig. 9 PL mapping, Se concentration calculated by PL data, EMS data, and XRD data of CG-248/InL-M0. (a) EPMA positions on PL mapping, (b) XRD positions on PL mapping, (c) Se concentration calculated by PL mapping, (d)–(i) EPMA-WDS results, atomic percentage (At) for each element in selected area; (j)—(k) XRD results.

structural properties influenced by cooling profiles. The results reveal that high Se segregation and the presence of defects, such as twin boundaries and stacking faults resulting from rapid cooling profiles, can collectively contribute to an increase in the PL bandgap.

In summary, this research not only highlights the unique properties and attributes of CST crystals but also firmly establishes them as a compelling and practical alternative to CdTe for solar applications. Beyond their immediate practical advantages, the insights gained from this study have the potential to make a substantial and lasting impact on the field of solar energy.

References

1. M.A. Scarpulla, B. McCandless, A.B. Phillips, Y. Yan, M.J. Heben, C. Wolden, G. Xiong, W.K. Metzger, D. Mao, D. Krasikov, I. Sankin, S. Grover, A. Munshi, W. Sampath, J.R. Sites, A. Bothwell, D. Albin, M.O. Reese, A. Romeo, M. Nardone, R. Klie, J.M. Walls, T. Fiducia, A. Abbas, and S.M. Hayes, CdTe-Based Thin Film Photovoltaics: Recent Advances, Current Challenges and Future Prospects. *Sol. Energy Mater. Sol. Cells* 255, 112289 (2023).

2. A. Nagaoka, D. Kuciauskas, J. McCoy, and M.A. Scarpulla, High P-Type Doping, Mobility, and Photocarrier Lifetime in Arsenic-Doped CdTe Single Crystals. *Appl. Phys. Lett.* 112, 192101 (2018).

3. J.J. Loferski, Theoretical Considerations Governing the Choice of the Optimum Semiconductor for Photovoltaic Solar Energy Conversion. *J. Appl. Phys.* 27, 777 (2004).

4. W. S. Queisser Hans, *Detailed Balance Limit of Efficiency of p–n Junction Solar Cells*, in *Renewable Energy* (Routledge, 2011).

5. C.H. Henry, Limiting Efficiencies of Ideal Single and Multiple Energy Gap Terrestrial Solar Cells. *J. Appl. Phys.* 51, 4494 (2008).

6. R. Mallick, X. Li, C. Reich, X. Shan, W. Zhang, T. Nagle, L. Bok, E. Bicakci, N. Rosenblatt, D. Modi, R. Farshchi, C. Lee, J. Hack, S. Grover, N. Wolf, W.K. Metzger, D. Lu, and G. Xiong, Arsenic-Doped CdSeTe Solar Cells Achieve World Record 22.3% Efficiency. *IEEE J. Photovolt.* 13, 510 (2023).

7. S. Krum and S. Haymore, *First Solar Achieves World Record 18.6% Thin Film Module Conversion Efficiency*, (2015).

8. J.R. Sites, Quantification of Losses in Thin-Film Polycrystalline Solar Cells. *Sol. Energy Mater. Sol. Cells* 75, 243 (2003).

9. J.M. Burst, J.N. Duenow, D.S. Albin, E. Colegrove, M.O. Reese, J.A. Aguiar, C.-S. Jiang, M. Patel, M.M. Al-Jassim, and D. Kuciauskas, CdTe Solar Cells with Open-Circuit Voltage Breaking the 1 V Barrier. *Nat. Energy* 1, 1 (2016).

10. R.W. Birkmire and B.E. McCandless, CdTe Thin Film Technology: Leading Thin Film PV into the Future. *Curr. Opin. Solid State Mater. Sci.* 14, 139 (2010).

11. H. Zhao, A. Farah, D. Morel, and C.S. Ferekides, The Effect of Impurities on the Doping and V_{OC} of CdTe/CdS Thin Film Solar Cells. *Thin Solid Films* 517, 2365 (2009).

12. N. Muthukumarasamy, S. Jayakumar, M.D. Kannan, and R. Balasundaraprabhu, Structural Phase Change and Optical Band Gap Bowing in Hot Wall Deposited $CdSe_xTe_{1-x}$ Thin Films. *Sol. Energy* 83, 522 (2009).

13. N.R. Paudel and Y. Yan, Enhancing the Photo-Currents of CdTe Thin-Film Solar Cells in Both Short and Long Wavelength Regions. *Appl. Phys. Lett.* 105, 183510 (2014).

14. D.E. Swanson, J.R. Sites, and W.S. Sampath, Co-Sublimation of $CdSe_xTe_{1-x}$ Layers for CdTe Solar Cells. *Sol. Energy Mater. Sol. Cells* 159, 389 (2017).

15. J.D. Poplawsky, W. Guo, N. Paudel, A. Ng, K. More, D. Leonard, and Y. Yan, Structural and Compositional Dependence of the $CdTe_xSe_{1-x}$ Alloy Layer Photoactivity in CdTe-Based Solar Cells. *Nat. Commun.* 7, 1 (2016).

16. C. Hagendorf, M. Ebert, M. Raugei, D. Lincot, J. BEngoechea, M. Rodriguez, and A. Lagunas, Assessment of Performance, Environmental, Health and Safety Aspects of First Solar's CdTe PV Technology, Fraunhofer Inst. Oxf. Brookes Univ. CNRS CENER (2017).

17. U. Roy, A. Bolotnikov, G. Camarda, Y. Cui, A. Hossain, K. Lee, W. Lee, R. Tappero, G. Yang, and R. Gul, High Compositional Homogeneity of $CdTe_xSe_{1-x}$ Crystals Grown by the Bridgman Method, APL Mater. **3**, 026102 (2015).

18. K. Zanio, Purification of CdTe from, Tellurium-Rich Solutions. *J. Electron. Mater.* 3, 327 (1974).

19. K. Kim, J. Hong, and S. Kim, Electrical Properties of Semi-Insulating $CdTe_{0.9}Se_{0.1}$: Cl Crystal and Its Surface Preparation. *J. Cryst. Growth* 310, 91 (2008).

20. S. Al-Heniti and A. Al-Hajry, Lattice Thermal Expansion of $CdTe_{0.9}Se_{0.1}$ Solid Solution. *J. Alloys Compd.* 387, L5 (2005).

21. F. Bassani, K. Saminadayar, S. Tatarenko, K. Kheng, R.T. Cox, N. Magnea, and C. Grattepain, Indium Doping of CdTe Layers and CdTe/$Cd_{1-x}Zn_x$Te Microstructures. *J. Cryst. Growth* 117, 391 (1992).

22. F. Bassani, S. Tatarenko, K. Saminadayar, N. Magnea, R. Cox, A. Tardot, and C. Grattepain, Indium Doping of CdTe and $Cd_{1-x}Zn_x$Te by Molecular-beam Epitaxy: Uniformly and Planar-doped Layers, Quantum Wells, and Superlattices. *J. Appl. Phys.* 72, 2927 (1992).

23. R. Grill, P. Fochuk, J. Franc, B. Nahlovskyy, P. Höschl, P. Moravec, Z. Zakharuk, Y. Nykonyuk, and O. Panchuk, High-temperature Defect Study of Tellurium-Enriched CdTe. *Phys. Status Solidi B* 243, 787 (2006).

24. S.K. Swain, J.N. Duenow, S.W. Johnston, M. Amarasinghe, J.J. McCoy, W.K. Metzger, and K.G. Lynn, Approach to Defect-Free Lifetime and High Electron Density in CdTe. *J. Electron. Mater.* 48, 4235 (2019).

25. P. Fochuk, O. Panchuk, P. Feychuk, L. Shcherbak, A. Savitskyi, O. Parfenyuk, M. Ilashchuk, M. Hage-Ali, and P. Siffert, Indium Dopant Behaviour in CdTe Single Crystals. *Nucl. Instrum.*

Methods Phys. Res. Sect. Accel. Spectrom. Detect Assoc. Equip. 458, 104 (2001).

26. S. Tatarenko, F. Bassani, K. Saminadayar, R. Cox, P. Jouneau, and N. Magnea, Indium Doping of (001), (111) and (211) CdTe Layers Grown by Molecular Beam Epitaxy. *J. Cryst. Growth* 127, 318 (1993).

27. G. Karczewski, A. Zakrzewski, L. Dobaczewski, W. Dobrowolski, E. Grodzicka, J. Jaroszyński, T. Wojtowicz, and J. Kossut, Properties of Epitaxially Grown CdTe Layers Doped with Indium. *Thin Solid Films* 267, 79 (1995).

28. S. Seto, K. Suzuki, V.N. Abastillas Jr., and K. Inabe, Compensating Related Defects in In-Doped Bulk CdTe. *J. Cryst. Growth* 214–215, 974 (2000).

29. W. Mohammed, The Electrical Properties of Post-Deposition Annealed and as-Deposited In-Doped CdTe Thin Films. *Renew. Energy* 26, 285 (2002).

30. M. Türker, J. Kronenberg, M. Deicher, H. Wolf, T. Wichert, and ISOLDE-Collaboration, Formation of DX-Centers in Indium Doped CdTe, in (Springer, 2008), pp. 231–238.

31. X.-H. Zhao, S. Liu, Y. Zhao, C.M. Campbell, M.B. Lassise, Y.-S. Kuo, and Y.-H. Zhang, Electrical and Optical Properties of N-Type Indium-Doped CdTe/$Mg_{0.46}Cd_{0.54}$Te Double Heterostructures. *IEEE J. Photovolt.* 6, 552 (2016).

32. T.K. Al-Hamdi, S.W. McPherson, S.K. Swain, J. Jennings, J.N. Duenow, X. Zheng, D.S. Albin, T. Ablekim, E. Colegrove, M. Amarasinghe, A. Ferguson, W.K. Metzger, C. Szeles, and K.G. Lynn, CdTe Synthesis and Crystal Growth Using the High-Pressure Bridgman Technique. *J. Cryst. Growth* 534, 125466 (2020).

33. J. Shang, M. Murugesan, S. Bigbee-Hansen, S.K. Swain, J.N. Duenow, S. Johnston, S.P. Beckman, H.H. Walker, R.W. Antonio, and J.S. McCloy, The Effect of Dopant Concentration and Annealing Treatments on N-Type Iodine Doped CdTe. *J. Alloys Compd.* 960, 170625 (2023).

34. A. Canul, D. Thapa, J. Huso, L. Bergman, R.V. Williams, and R. Machleidt, Mixed-Strategy Approach to Band-Edge Analysis and Modeling in Semiconductors. *Phys. Rev. B* 101, 195308 (2020).

35. T.C.M. Santhosh, K.V. Bangera, and G.K. Shivakumar, Synthesis and Band Gap Tuning in $CdSe_{(1-x)}Te_{(x)}$ Thin Films for Solar Cell Applications. *Sol. Energy* 153, 343 (2017).

36. A.J. Strauss and J. Steininger, Phase Diagram of the CdTe-CdSe Pseudobinary System. *J. Electrochem. Soc.* 117, 1420 (1970).

37. A. Verma and P. Krishna, Polymorphism and Polytypism in Crystals, John Wiley Sons Inc., (1966).

38. S. Mardix, Polytypism: A Controlled Thermodynamic Phenomenon. *Phys. Rev. B* 33, 8677 (1986).

39. J. McCloy and R. Korenstein, Variability in Chemical Vapor Deposited Zinc Sulfide: Assessment of Legacy and International CVD ZnS Materials, in Vol. 7302 (SPIE, 2009), pp. 199–206.

40. K. Ohata, J. Saraie, and T. Tanaka, Phase Diagram of the CdS-CdTe Pseudobinary System. *Jpn. J. Appl. Phys.* 12, 1198 (1973).

41. S. Patil and P. Pawar, Structural and Optical Studies of Thermally Evaporated $CdSe_XTe_{1-X}$ Thin Films. *J. Chem. Biol. Phys. Sci. JCBPS* 2, 1472 (2012).

42. R. Kharabe, S. Jadhav, A. Shaikh, D. Patil, and B. Chougule, Magnetic Properties of Mixed Li–Ni–Cd Ferrites. *Mater. Chem. Phys.* 72, 77 (2001).

43. K. Sharma, A.S. Al-Kabbi, G.S.S. Saini, and S.K. Tripathi, Indium Doping Induced Modification of the Structural, Optical and Electrical Properties of Nanocrystalline CdSe Thin Films. *J. Alloys Compd.* 564, 42 (2013).

44. J.S. McCloy, J.V. Ryan, T. Droubay, T.C. Kaspar, S. Chambers, and D.C. Look, Magnetotransport Properties of High Quality Co:ZnO and Mn:ZnO Single Crystal Pulsed Laser Deposition Films: Pitfalls Associated with Magnetotransport on High Resistivity Materials. *Rev. Sci. Instrum.* 81, 063902 (2010).

45. J. D. Friedl, E. Bastola, R. A. Awni, X. Mathew, A. B. Phillips, Y. Yan, and M. J. Heben, Influence of Se Grading on the Free Carrier Profile of CdSeTe/CdTe Solar Cells, in 2022 IEEE 49th Photovoltaics Specialists Conference (PVSC) (2022), pp. 0761–0765.

46. D. R. Lide, CRC Handbook of Chemistry and Physics, Vol. 85 (CRC press, 2004).

47. W.M.H. Sachtler, G.J.H. Dorgelo, and A.A. Holscher, The Work Function of Gold. *Surf. Sci.* 5, 221 (1966).

48. S.A. Fayek and S.M. El-Sayed, Characterization of Short-Range Order in an Amorphous Cd–Se–Te System by Wide Angle X-Ray Scattering(WAXS). *NDT E Int.* 36, 619 (2003).

49. F. Peiris, Z. Weber, Y. Chen, and G. Brill, Optical Properties of $CdSe_xTe_{1-x}$ Epitaxial Films Studied by Spectroscopic Ellipsometry. *J. Electron. Mater.* 33, 724 (2004).

50. J.S. McCloy, R. Korenstein, and B. Zelinski, Effects of Temperature, Pressure, and Metal Promoter on the Recrystallized Structure and Optical Transmission of Chemical Vapor Deposited Zinc Sulfide. *J. Am. Ceram. Soc.* 92, 1725 (2009).